OPEN ACCESS

ACTA METALLURGICA SLOVACA

2025, VOL. 31, NO. 4, 253-258

SCICELL

RESEARCH PAPER

Effect of high-carbon austenite content at different niobium concentrations on the mechanical properties of austempered ductile iron

César Yeshua Becerra Mayorga[1], Cynthia Aristeo Domínguez[1], José Merced Martínez Vázquez[2], Erick Uriel Morales Cruz[1], Demetrio Fuentes Hernández[1], Edgar Cardoso Legorreta[1], Marissa Vargas Ramírez[1]

[1] Universidad Autónoma del Estado de Hidalgo, Área Académica de Ciencias de la Tierra y Materiales, Pachuca-Tulancingo Km. 4.5, Carboneras, 42184, Hidalgo, México.
[2] Universidad Politécnica de Juventino Rosas, Hidalgo 102, Comunidad de Valencia, 38253, Juventino Rosas, Guanajuato, México.
*Corresponding author: cesar_becerra@uaeh.edu.mx, tel.: +52 7713169702, Área Académica de Ciencias de la Tierra y Materiales, Pachuca-Tulancingo Km. 4.5, Carboneras, 42184, Hidalgo, México.

Received: 11.09.2025
Accepted: 14.11.2025

ABSTRACT

This study explores the influence of high-carbon retained austenite content, as modulated by niobium additions and austempering time, on the hardness, wear resistance, and impact toughness of ductile iron. Four alloys containing 0, 0.1, 0.2, and 0.3 wt.% niobium were austempered at a constant temperature of 350 °C for 15, 30, 60, and 90 minutes. Alloys with higher niobium contents (0.2 and 0.3%) reached their maximum retained austenite fractions at 30 minutes (40.67 and 41.98%, respectively), while the 0 and 0.1% niobium alloys exhibited their peak values at 60 minutes. Regarding mechanical properties, the highest hardness was obtained in Sample 2 after 30 minutes of austempering (37.5 HRC), whereas the highest absorbed impact energy was observed in Sample 3 under the same conditions (16 J). Consequently, a higher fraction of high-carbon retained austenite provides an optimal balance between hardness and wear resistance without a significant loss in impact toughness.

Keywords: High-carbon retained austenite; niobium; austempering; austempered ductile iron.

INTRODUCTION

Ductile iron (DI) consists of graphite nodules dispersed within a ferritic-pearlitic matrix. These materials are widely recognized for their excellent mechanical performance and cost-effectiveness [1]. Due to their good ductility, toughness and lower density, ductile irons have the potential to replace steels in certain applications [2], particularly in the automotive industry, where they are commonly used in components such as crankshafts, valves and axles [3,4].

Austempered ductile iron (ADI) is a modified form of DI that undergoes an isothermal heat treatment designed to enhance its mechanical properties. The heat treatment involves two main stages: austenitizing -typically at 900°C- to stabilize a carbon-enriched austenite phase, followed by quenching into a salt bath maintained between 250 °C and 380 °C to promote a diffusion- controlled transformation known as austempering [5-8]. During austempering, the proportions of ferrite and austenite in the matrix change considerably, directly influencing the material´s mechanical response [9]. Like other diffusional transformations, austempering kinetics are governed by both time and temperature. Several studies have investigated the role of these parameters in shaping the microstructure and phase distribution of ADI [10]. This transformation results in a microstructure known as ausferrite, which forms through the nucleation and growth of ferrite within retained austenite. The formation and stability of this structure are highly sensitive to chemical composition, austempering conditions and the size and dispersion of graphite nodules [11]. The austempering temperature strongly influences the resulting microstructure. Higher temperatures (350-400 °C) typically yield ADI with lower hardness and strength but superior ductility and fracture toughness, due to the formation of significant amounts (20-40%) of high-carbon retained austenite [12]. In contrast, lower austempering temperatures (below 350 °C) favor enhanced wear resistance, albeit at the expense of impact resistance [13]. With increased austempering time, the fraction of acicular ferrite tends to rise, while the volume of high-carbon austenite initially increases before gradually decreasing. This evolution generally leads to improved tensile properties and impact toughness but reduces hardness and wear resistance [14]. However, excessively high austempering temperatures can trigger secondary reactions in which high-carbon austenite decomposes into bainitic ferritic and carbides, negatively affecting both ductility and impact performance [15]. For instance, ausferrite can form in as little as 30 minutes at 400 °C, whereas at 230 °C the transformation may require up to 4 hours to complete [16]. Niobium is an emerging alloying addition in ductile irons, with several studies reporting favorable effects on both microstructural development and mechanical behavior. Chen et al. [17] reported improved mechanical properties – including a yield strength of 418 MPa, ultimate tensile strength of 746 MPa and elongation of 8%- in ductile iron with 0.08% Nb. Ahmed et al. [18] noted that niobium accelerates the formation of ausferrite during austempering. Similarly, Sckudlarek et al. [19] studied a ductile iron alloyed with 0.35% Nb and found that niobium promotes pearlite formation and acts as a potent carbide former. They observed that the best combination of ultimate tensile strength (1150 MPa) and ductility (5%) was achieved after 60 minutes of austempering at 360 °C. Abdullah et al. [20] also reported a direct correlation between austempering time and increased hardness, reaching a maximum of 41.27 HRC after three hours.

Niobium plays a complex role in the microstructural evolution of austempered ductile iron (ADI). As a strong carbide-forming element, niobium readily combines with carbon to form stable niobium carbides (NbC) during solidification and austenitization, thereby significantly influencing the subsequent austempering transformation. On one hand, these carbides act as heterogeneous nucleation sites for ferrite, refining the ausferritic microstructure and improving hardness and wear resistance. Several authors [21,22] have also observed improved abrasive wear resistance for Nb additions up to 1.48 wt.%. This improvement is primarily attributed to the refinement of pearlite interlamellar spacing, the reduction of austenitic grain size, and the formation of NbC nano-precipitates within the matrix, all of which contribute to enhanced hardness and tensile strength [23]. Pimentel and Guesser [24] also observed that Nb promotes the formation of primary carbides that persist after austempering, contributing to microstructural heterogeneity and potentially impairing ausferrite uniformity. Therefore, while niobium enhances hardenability and wear resistance, its strong affinity for carbon must be carefully controlled to avoid compromising the development of the ausferritic matrix.

The present study aims to evaluate how variations in high-carbon retained austenite content—modulated by different niobium concentrations (0–0.32 wt.%) and austempering durations (15, 30, 60, and 90 min)—affect the mechanical properties of austempered ductile iron (ADI). An austempering temperature of 350 °C was selected because it promotes the formation of a coarse ausferritic structure with a higher fraction of high-carbon retained austenite, providing a balanced combination of hardness, ductility, and wear resistance.

The novelty of this study lies in the systematic quantification of high-carbon retained austenite across multiple austempering times and niobium concentrations, as well as the establishment of a direct correlation between the evolution of this phase and the resulting mechanical behavior. In contrast to previous works that

investigated similar thermal conditions (900 °C / 350 °C / 30–60 min), this research introduces a broader time range (15–90 min) to reveal the kinetics of austenite stabilization and decomposition. Furthermore, the dual role of niobium—as a carbide-forming element that limits carbon solubility and as a grain refiner that enhances ausferrite nucleation—is critically analyzed. This integrated approach provides new insights into how controlled niobium additions influence the balance between hardness, impact toughness, and wear resistance in ADI, contributing valuable information for the optimization of industrial heat-treatment schedules.

MATERIAL AND METHODS

Ductile iron

The ductile iron alloys were produced using 1018 steel and returned ductile iron as the base materials. Composition adjustments were made through the addition of ferrosilicon, ferroniobium, and a silicon-magnesium ferroalloy, the latter serving as a nodulizing agent to promote the formation of spheroidal graphite. Carbon content was regulated using pure graphite powder. The chemical compositions of the resulting alloys are summarized in **Table 1**. After solidification and cooling, the castings were sectioned into 4 cm cubic specimens for subsequent heat treatment.

Table 1 Chemical composition of the ductile iron alloys.

Element (%)	DI 0% Nb (Sample 1)	DI 0.1% Nb (Sample 2)	DI 0.2% Nb (Sample 3)	DI 0.3% Nb (Sample 4)
Carbon	3.76	3.62	3.71	3.67
Silicon	2.54	2.64	2.51	2.61
Manganese	0.38	0.32	0.37	0.32
Sulfur	0.03	0.03	0.02	0.02
Phosphorus	0.009	0.007	0.006	0.009
Niobium	0	0.11	0.23	0.32
Iron	Balance	Balance	Balance	Balance

Austempering heat treatment

The austempering process was conducted in two stages. First, the samples were austenitized at 900 °C for 1 h to ensure the formation of a fully austenitic matrix. After austenitization, the specimens were transferred to a second furnace containing a salt bath composed of an equimolar mixture of potassium nitrate and sodium nitrate, maintained at 350 °C. Additional salt was added as required during the process to keep the samples completely submerged. Austempering durations of 15, 30, 60, and 90 min were applied. At the end of each treatment cycle, the samples were quenched in water at room temperature to preserve the ausferritic microstructure.

Metallographic analysis

Phase identification and microstructural characterization were carried out using two complementary techniques. First, optical microscopy was performed with a Keyence digital microscope. The samples were metallographically prepared by sequential grinding with SiC abrasive papers (grit sizes ranging from 50 to 2000), followed by polishing with 1 and 0.5 µm diamond suspensions. The ausferritic microstructure—composed of acicular ferrite and high-carbon retained austenite—was revealed by etching with a 4% nital solution. Carbides were identified by etching with a 10% ammonium persulfate solution. The nodular size of the samples was determined using Equation (1).

$$NS_{avg} = 2\sqrt{A\pi^{-1}} \quad (1.)$$

Where: A [µm^2] – Area of nodules with diameters larger than 10 µm

The inter-nodular spacing, which expresses the diffusion distance of carbon during the austempering process, was determined using Equation (2).

$$\lambda_G = 55.4\left(\frac{NS_{avg}}{P^2}\right) \quad (2.)$$

Where: P [µm] – Perimeter of the nodule

X-ray diffraction

Quantitative phase analysis was subsequently carried out via X-ray diffraction (XRD) using Co-Kα1 radiation. The volume fraction of high-carbon retained austenite was determined using Equation (3), based on the relative intensities and diffraction angles of the ferrite and austenite peaks.

$$Vy = \frac{1-Vc}{1+\left(\frac{\Sigma I\alpha}{\Sigma Iy}\right)\left(\frac{\Sigma Ry}{\Sigma R\alpha}\right)} \quad (3.)$$

Where: Vy [%] - High-carbon austenite volume fraction
Vc [%] - Carbides volume fraction
Iα [counts per second] – Intensity of the hkl plane of the α phase
Iγ [counts per second] – Intensity of the hkl plane of the γ phase
Rα [unitless] – α phase correction
Rγ [unitless] – γ phase correction

Correction factors for both the ferrite and austenite phases were calculated using Equation (4).

$$R = \left(\frac{1}{v^2}\right)[|F|^2 p(1+cos^2 2\theta)/(sin^2\theta cos\theta)](e^{-2M}) \quad (4.)$$

Where: v [Å^3] – Volume of the unit cell
F [unitless] – Number of crystallographic planes that produce reflections of the same intensity due to symmetry
Θ [°] – Bragg angle
M [unitless] – Debye- Waller temperature factor

For the function M, corresponding to the Debye–Waller temperature factor, Equation (5) was employed.

$$M = B\frac{Sin^2\theta}{\lambda^2} \quad (5.)$$

Where: B [unitless] – Material constant related to the Debye temperature
λ [Å] – Wavelength of the radiation source

Charpy impact test

Charpy impact testing was conducted in accordance with ASTM E23, using a 45° V-notch with a depth of 2 mm, positioned on the side opposite to the impact zone, and a standard pendulum impact tester. Reported values represent the average of four replicates per condition.

Wear test

Wear resistance was evaluated using a TE 53 SLIM multi-purpose friction and wear tester in a block-on-ring configuration without lubrication, at room

temperature, with sample surface roughness ranging from 0.4 to 1 µm. Testing followed the parameters defined in ASTM G77-05: 4000 cycles, 300 rpm rotational speed, and a load of 50 N. The volume loss was quantified using Equation (6) as specified in ASTM G132-96, shown below.

$$lost\ volume = \frac{D^2 t}{8}\left[2sin^{-1}\frac{b}{D} - \sin\left(2sin^{-1}\frac{b}{D}\right)\right] \quad (6.)$$

Where: D [mm] – Ring diameter
t (mm) – Specimen width
b (mm) – Average width of the wear scar

Hardness test

Hardness measurements were obtained using a Buehler universal hardness tester equipped with a diamond indenter and a 150 kgf load. All measurements were recorded on the Rockwell C scale, with reported values representing the average of 10 readings taken from different regions of each sample.

RESULTS AND DISCUSSION

Metallography of austempered ductile iron

The mechanical properties of austempered ductile irons (ADIs) are strongly influenced by the material's microstructure, particularly the presence of carbides, acicular ferrite, high-carbon retained austenite, and the morphology of graphite nodules. **Fig. 1** shows the carbides present in each sample. During the solidification of ductile iron, the addition of niobium promotes the precipitation of stable carbides, which act as nucleation sites for ausferrite (acicular ferrite and high-carbon retained austenite) and restrict grain growth. Carbide formation enhances the hardness and wear resistance of ADIs by reducing dislocation mobility. The quantification of these carbides is presented in Table 1, showing that Sample 1 (0% Nb) has the lowest carbide fraction (0.53%), while increasing the niobium content in the alloy leads to a corresponding increase in carbon content, reaching the highest fraction in Sample 4 (0.32% Nb, 2.48%).

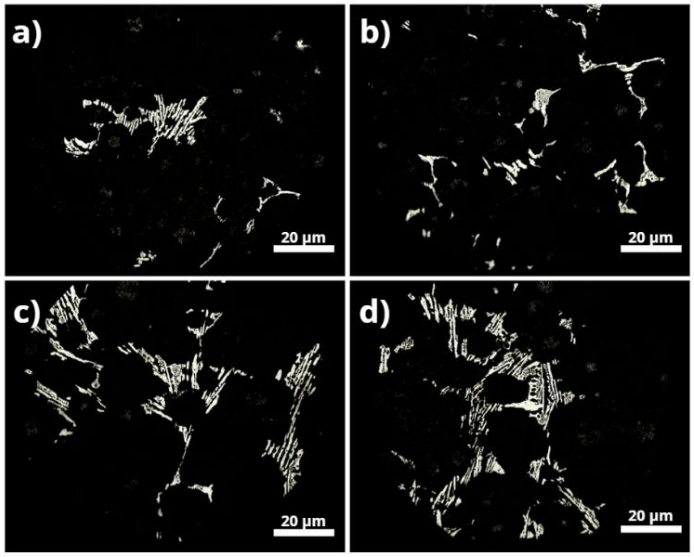

Fig. 1. Carbides in each of the samples: (a) Sample 1, (b) Sample 2, (c) Sample 3, and (d) Sample 4.

The graphite nodules shown in **Fig. 2** are crucial to the mechanical properties of ADIs. Their shape, size, distribution, and quantity directly affect the stability of high-carbon retained austenite. During austempering, the nodules act as carbon sources, diffusing into the austenitic matrix and enriching the austenite in carbon, thereby improving its stabilization during cooling. **Table 2** presents the graphite morphology results, indicating that higher niobium content decreases nodularity from 256.1 nodules/mm² in Sample 1 to 156.4 nodules/mm² in Sample 4. A high number of nodules tends to refine the microstructure, reducing the size of ferrite needles and increasing the austenite fraction. Inter-nodular spacing also influences the kinetics of austenite-to-ausferrite transformation. Smaller spacing (closely spaced nodules) promotes a homogeneous carbon distribution in the matrix, enhancing retained austenite stabilization, whereas larger spacing results in carbon-deficient regions where austenite can transform into bainite, producing a more heterogeneous microstructure.

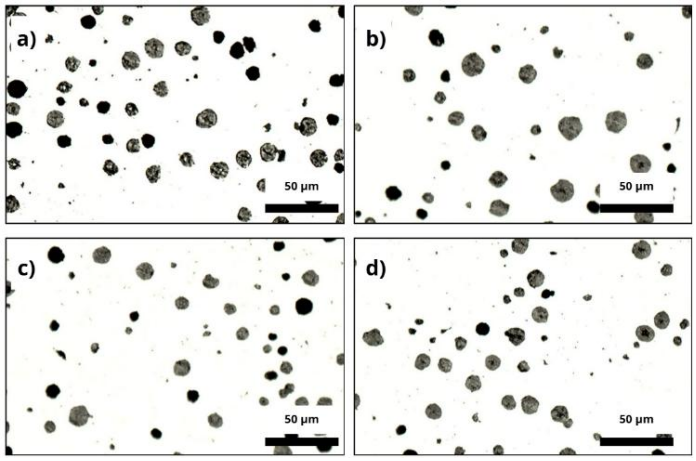

Fig. 2 Graphite nodules in each alloy: (a) Sample 1, (b) Sample 2, (c) Sample 3, and (d) Sample 4.

Table 2 Distribution of graphite nodules and carbides in the ductile iron alloys.

Property/alloy	Sample 1	Sample 2	Sample 3	Sample 4
Nodule size (µm)	21.72	29.96	26.56	23.23
Inter-nodular distance (µm)	23.92	35.51	33.51	29.33
Nodule count (nod/mm^2)	256.1	113.7	120.4	156.4
Graphite (vol.%)	8.03	6.95	6.11	6.65
Carbides (vol.%)	0.53	0.95	1.51	2.48

The microstructural analysis of the ADI revealed a typical ausferritic matrix, as illustrated in **Fig. 3**. The dark regions correspond to acicular ferrite, which exhibits a characteristic needle-like morphology. The interlocking structure of these ferrite needles provides substantial mechanical strength by impeding dislocation motion, thereby enhancing wear resistance [25]. In contrast, the lighter regions are attributed to high-carbon retained austenite, a metastable phase that persists after heat treatment. The stabilization of this phase is facilitated by carbon enrichment during the austenitization stage, which subsequently contributes to solid solution strengthening [26].

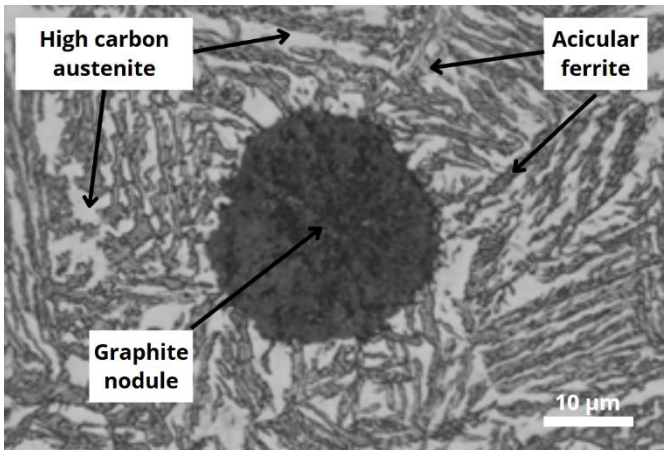

Fig. 3 ADI microstructure after 30 minutes at 350°C.

Fig. 4 presents representative micrographs of all four samples at different austempering times. The volume fraction of high-carbon austenite increases with austempering time, particularly between 15 and 60 minutes. This trend can be attributed to the progressive diffusion of carbon from ferrite into austenite, which stabilizes the austenite at room temperature. This stabilization suppresses further ferrite nucleation and growth. However, excessive austempering times may lead to carbide precipitation, potentially compromising the material's toughness and ductility [14].

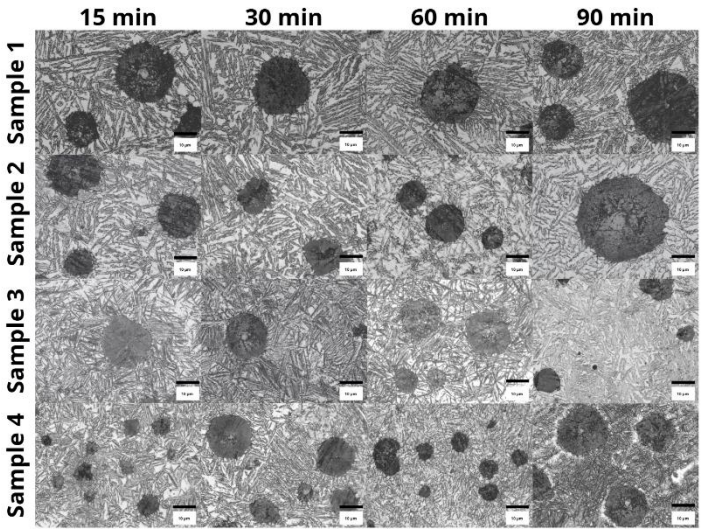

Fig 4. Microstructures of simples 1, 2, 3 and 4 subjected to austempering heat treatment from 15 to 90 minutes.

X-ray diffraction

To quantify the phase fractions more accurately, X-ray diffraction (XRD) analysis was performed. **Fig. 5** presents a general diffractogram of the austempered ductile irons with carbides, while **Fig. 6** shows the diffractograms of the individual samples. The results shown in **Fig. 7** indicate that alloys containing 0.2 and 0.3% Nb (Samples 3 and 4) achieved the highest retained austenite content at 30 minutes of austempering (40.67% and 41.98%, respectively). In contrast, the Nb-free alloy and the 0.1% Nb alloy (Samples 1 and 2) exhibited maximum retained austenite at 60 minutes. This behavior is attributed to niobium's dual role in the alloy: first, as a strong carbide-forming element (forming NbC), it reduces carbon solubility in the matrix and enriches the remaining austenite in carbon, thereby enhancing its stability; second, as a grain refiner, niobium promotes uniform ausferrite formation by increasing nucleation sites [27].

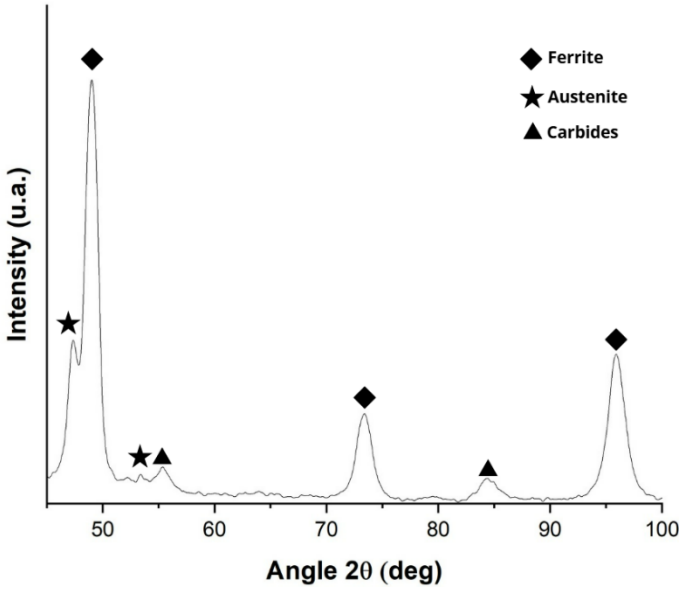

Fig 5. X-ray diffractogram of ADI at 30 minutes and 350 °C.

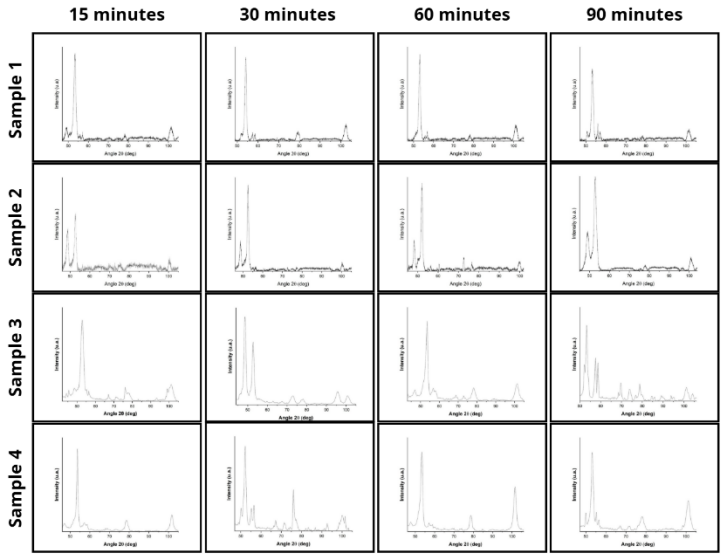

Fig 6. X-ray diffractograms of the austempered samples with different niobium contents.

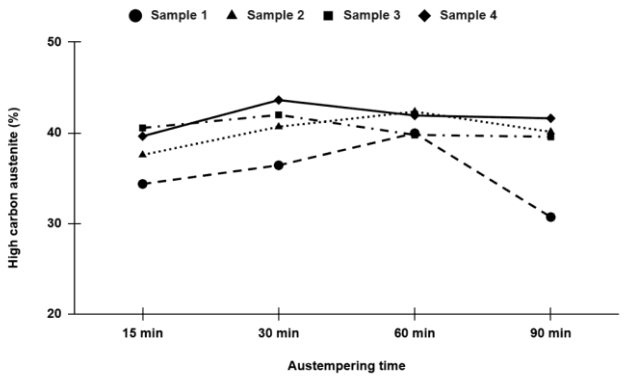

Fig 7. High-carbon retained austenite percentage in the four samples as a function of austempering time.

Hardness testing

A clear inverse correlation between hardness and retained austenite content is evident in **Fig. 8**. Higher amounts of retained austenite result in lower hardness values, given the relatively ductile nature of this phase compared to acicular ferrite. As austempering time progresses, the retained austenite partially decomposes into bainitic ferrite and carbides, thereby improving hardness by increasing the obstruction to dislocation movement [28,29]. This effect is particularly noticeable in samples 3 and 4 between 30 and 60 minutes, where hardness increases from 25.56 to 25.98 HRC and from 26.48 to 28.76 HRC, respectively. Similarly, in samples 1 and 2, a notable rise in hardness is observed between 60 and 90 minutes, from 25.2 to 28.6 HRC in sample 1 and from 22.54 to 27.1 HRC in sample 2. These observations suggest that the transformation of retained austenite into harder phases occurs earlier in the alloys with higher niobium content.

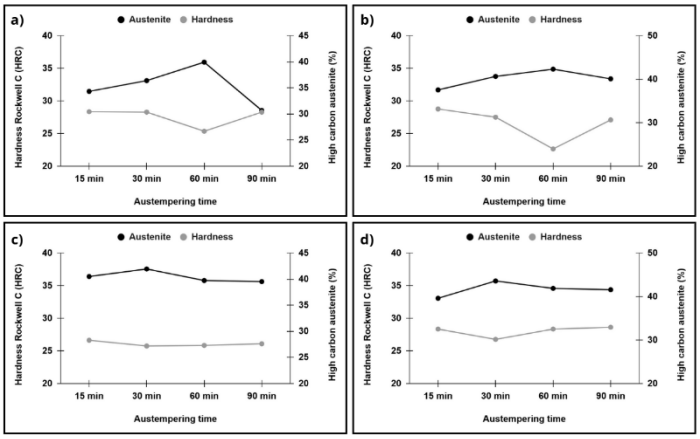

Fig. 8 Relationship between hardness and high-carbon retained austenite content: (a) sample 1, (b) sample 2, (c) sample 3 and (d) sample 4.

Fig. 9 shows the indentations and their depths. Indentation depth is inversely proportional to material hardness, meaning that higher hardness corresponds to shallower indentations. Consequently, an increase in niobium content results in greater carbide formation, which acts as a barrier to dislocation motion, thereby increasing hardness.

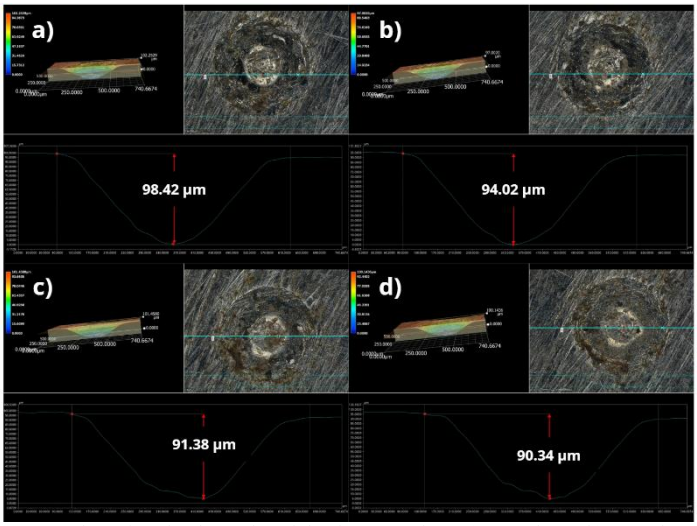

Fig 9. Indentation depth results of the four samples: (a) Sample 1, (b) Sample 2, (c) Sample 3, and (d) Sample 4.

Wear testing

Wear resistance, assessed through volume loss, is depicted in **Fig. 10**. Samples 3 and 4 exhibited retained austenite content. Since austenite is more prone to plastic deformation and adhesive wear, its prevalence in the microstructure results in greater material loss. However, by 90 minutes, wear volume decreases across all alloys, a trend consistent with the transformation of retained austenite into harder bainitic ferrite and carbides. Despite their beneficial effect on wear resistance, coarse or clustered carbides may compromise surface integrity by acting as sites for crack initiation and particle detachment [30].

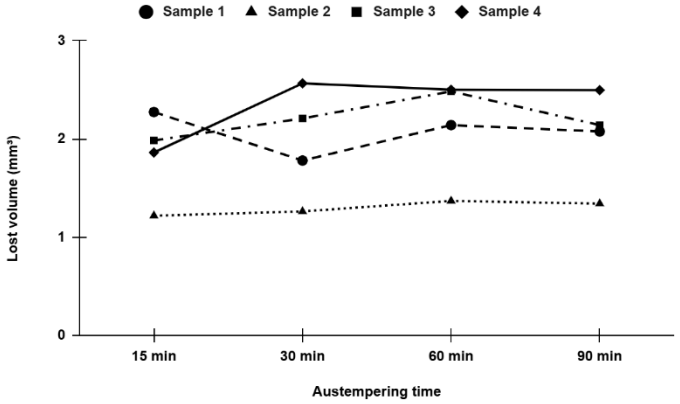

Fig. 10. Volume loss in simples 1, 2, 3 and 4 as a function of austempering time.

Fig. 11 shows the wear profiles of the thermally treated samples. The greatest wear depths were observed in the samples with the highest content of high-carbon retained austenite, as retained austenite is a more ductile phase than acicular ferrite. After 90 minutes of austempering, the system enters the second austempering reaction, in which retained austenite transforms into bainitic ferrite and carbides. Both phases exhibit higher hardness, resulting in shallower indentation depths.

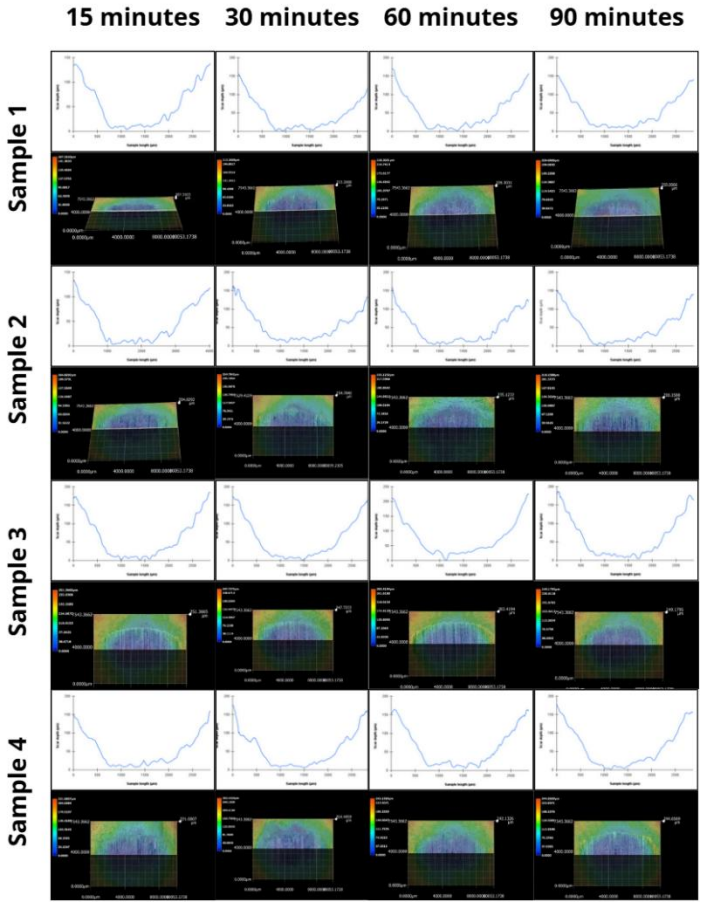

Fig 11. Wear profiles of the austempered ductile iron alloys.

Charpy impact testing

Impact energy results are presented in **Fig. 12**. Samples 1 and 2 exhibit lower absorbed energies overall, with sample 1 reaching a minimum of 10 J at 15 minutes. In contrast, sample 3 and 4 are attributed to the higher retained austenite content, which absorbs impact energy more effectively due to its ductility [31]. However, this beneficial effect diminishes at longer austempering durations due to the formation of brittle carbides, which act as stress concentrators and facilitate crack propagation [32]. This behavior is evident in sample 4 at 90 minutes, where the higher niobium content leads to increased carbide formation and a corresponding decrease in impact toughness compared to sample 3.

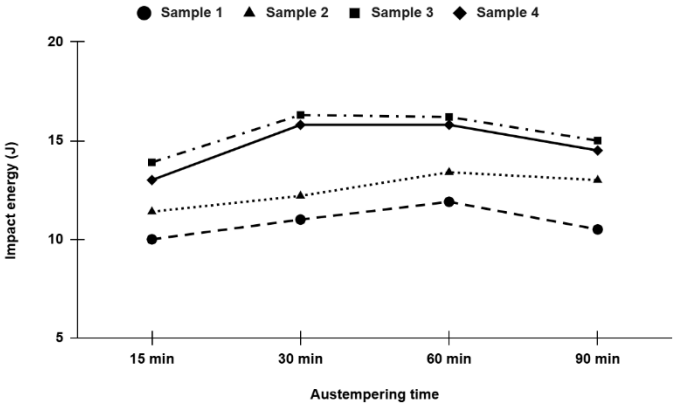

Fig. 12. Effect of austempering time on impact energy for samples 1–4

CONCLUSIONS

This study evaluated the effect of high-carbon retained austenite content on niobium-alloyed ADI as a function of austempering time. Niobium addition promoted faster formation of carbon-enriched retained austenite, with samples 3 and 4 reaching maximum values at 30 minutes (40.67% and 41.98%). Higher retained austenite fractions corresponded to lower hardness. At the same time, impact energy peaked in samples 1 and 2 at 60 minutes (11.9 and 13.4 J) and in samples 3 and 4 at 30 minutes (16.3 and 15.8 J), demonstrating the stabilizing effect of this phase. After 90 minutes, wear volume decreased due to decomposition of high-carbon austenite into bainitic ferrite and carbides.

Although limited by sample size and measurement precision, these trends align with literature on Nb-alloyed ADI, where NbC precipitates nucleate ausferrite and influence properties. Compared to previous studies, this work demonstrates higher retained austenite contents (~42% vs. ~33%) and greater impact energies, surpassing values reported in similar ADI alloys (~10–14 J), while providing a more precise correlation between microstructure and mechanical properties and a thorough assessment of wear behavior across austempering times. These findings are industrially relevant, offering guidance to optimize hardness, toughness, and wear resistance in components such as automotive gears, suspension parts, and mining machinery.

Notable observations include the accelerated stabilization of retained austenite with niobium addition and its correlation with peak impact energy, providing valuable insight for designing industrial heat treatment schedules to enhance performance.

Acknowledgements: The authors express their sincere gratitude to the Secretaría de Ciencia, Humanidades, Teconología e Innovación (SECIHTI), the Universidad Autónoma del Estado de Hidalgo (UAEH) and the Instituto Politécnico Nacional (IPN) for their financial and technological support, which made this research possible.

REFERENCES

1. L. Horbach et al.: Materials & Design, 244, 2024, 113130. https://doi.org/10.1016/j.matdes.2024.113130
2. S.R. Soria, X.H. Li, M. Schulz, M. Boin, C. Broeckmann: Materials Characterization, 116, 2020, 110453. https://doi.org/10.1016/j.matchar.2020.110453
3. J.O. Olawale, S.A. Ibitoye, K.M. Oluwasegun: International Journal of Science and Engineering Research, 7 (9), 2016, 397-423.
4. W. Stets, L. Blich, G. Gassner, P. Schumacher: Journal of Metalcasting, 8, 2014, 21-27. https://doi.org/10.1007/BF03355568
5. J.F. Janowak, R.B. Gundlach, G.T. Eldis, K. Rohrting: International Cast Metals Journal, 6, 1982, 28–42.
6. T.N. Rouns, K.B. Rundman, D.M. Moore: AFS Transactions, 121, 1984, 815-840.
7. W. Dubensky, K.B. Rundman: AFS Transactions, 93, 1985, 389-394.
8. J.F. Janowak, P.A. Norton: AFS Transactions, 88, 1985, 123-125.
9. O.J. Akinribide et al.: Materials, 15 (20), 2022, 7109. https://doi.org/10.3390/ma15207109
10. P. Keizlar Z. Andrsova, M. Petrzilkova, B. Skrbek, A. Duchac, D. Myszka: Materials Science Forum, 1081, 2023, 125-130. https://doi.org/10.4028/p-7xl336
11. L. Meier, M. Hofmannm P. Saal, W. Volk, H. Hoffmann: Materials Characterization, 85, 2013, 124-133. https://doi.org/10.1016/j.matchar.2013.09.005
12. C.H. Hsu, Y.H. Shy, Y.H. Yu, S.C. Lee: Materials Chemistry and Physics, 63 (1), 2000, 75-81. https://doi.org/10.1016/S0254-0584(99)00213-8
13. Y.J. Kim, H. Shin, H. Park, J.D. Lim: Materials Letters, 62 (3), 2008, 357–360. https://doi.org/10.1016/j.matlet.2007.05.028
14. Z. Shi M. Dong, Y. Sun, J. Ma, X. Du, J. Zhao: Metallurgical Research & Technology, 119 (1), 2022, 117. https://doi.org/10.1051/metal/2022011
15. L.F.V. Guerra, A.B. Jacuinde, I. Mejia, J. Zuno, C. Maldonado: Materials Science and Engineering: A, 648, 2015, 193-201. https://doi.org/10.1016/j.msea.2015.09.066
16. J.F. Dias, G.O. Ribeiro, D.J. Carmo, J.J. Vilela:Materials Science and Engineering: A, 556, 2012, 408-413. https://doi.org/10.1016/j.msea.2012.07.005
17. X. Chen et al.: Materials Science and Engineering: A, 688, 2017, 416-428. https://doi.org/10.1016/j.msea.2017.01.032
18. M. Ahmed, M. Soliman, M. Youseff, R. Bähr, A. Nofal: Metals, 11 (5), 2021, 703. https://doi.org/10.3390/met11050703
19. W. Sckudlarek, M.N Krmasha, K. S. Al-Rubaie, O. Preti, J.C.G. Milan, C.E. da Costa: Journal of Materials Research and Technology, 12, 2021, 2414-2425. https://doi.org/10.1016/j.jmrt.2021.04.041
20. B. Abdullah, S.K. Alias, A. Jaffar, R.W. Freddawati, A. Ramli: Advanced Materials Research, 418–420, 2011, 1768–1771. https://doi.org/10.4028/www.scientific.net/AMR.418-420.1768
21. Z. Wenbin, Z. Hongbo, Z. Dengke, Z. Hongxing, H. Qin, Z. Qijie: China Foundry, 8 (1), 2010, 36-40.
22. H. Mohrbacher, Q. Zhai: Niobium alloying in grey cast iron for vehicle brake discs, *Proc. of Materials Science & Technology Conf.*, USA, 2011.
23. E. Campomanes: AFS Transactions, 73 (8), 1973, 122-123.
24. A. Pimentel, W. Guesser: Revista Materia, 22 (2), 2017. https://dx.doi.org/10.1590/S1517-707620170002.0148
25. B. Avishan, M. Charchi-Aghdam, M.H. Khanmiri: International Journal of Metalcasting, 2025. https://doi.org/10.1007/s40962-025-01604-9
26. M. Morawic, V. Ruiz-Jimenez, C. Garcia-Mateo: Journal of Thermal Analysis and Calorimetry, 142, 2020, 1709-1719. https://doi.org/10.1007/s10973-020-10259-z
27. X. Chen et al.: Materials Science and Engineering: A, 760, 2019, 377–386. https://doi.org/10.1016/j.msea.2019.05.100
28. P. Yang, H. Fu, G. Li, J. Liu, X. Zhao: Materials & Design, 186, 2019, 108363. https://doi.org/10.1016/j.matdes.2019.108363
29. B. Wang, G.C. Barber, X. Sun, M.C. Shaw, P. Seaton: Journal of Materials Engineering and Performance, 26 (9), 2017, 4565–4574. https://doi.org/10.1007/s11665-017-2663-1
30. P. Sellamuthi, D.G.H. Samuel, D. Dinakaran, V.P. Premkumar, Z. Li, S. Seetharaman: Metals, 8 (1), 2018, 53. https://doi.org/10.3390/met8010053
31. S.S. Sharma, A. Hedge: Materials Research, 24 (6), 2021. https://doi.org/10.1590/1980-5373-MR-2021-0301
32. N. Fatahalla, O. Hussein: OALib Journal, 2 (3), 2015, 1–16.